光学学报

硫汞族量子点红外光电探测技术

郝群[1,2,3*]，唐鑫[1,2,3]，陈梦璐[1,2,3]

[1]北京理工大学光电学院，北京 100081；
[2]精密光电测试仪器及技术北京市重点实验室，北京 100081；
[3]北京理工大学长三角研究院，浙江 嘉兴 314019

摘要 受限于复杂的分子束外延生长及倒装键合工艺，现有块体半导体红外探测器成本高昂、工艺复杂、极大制约了成像阵列规模和分辨率的进一步提升。胶体量子点作为一种新兴的半导体纳米晶体材料，因"量子限域"效应，能够实现宽谱段范围内的精准带隙调控。同时，胶体量子点可通过液相化学合成方法低成本大批量制备。此外，胶体量子点的液相加工工艺使得其可以与硅基读出电路进行直接片上电学耦合，突破了倒装键合工艺限制。因此，胶体量子点在红外探测及成像领域展现了巨大的应用前景。其中硫汞族量子点具有探测波段范围宽、物性调控易及便于硅基集成等优势，先后实现了中波红外背景限探测、双色探测及焦平面阵列成像等，在红外光电技术展示了巨大的潜力。本综述总结了近年来硫汞族胶体量子点红外光电探测技术的研究现状，并对其未来发展方向进行了展望。

关键词 硫汞族胶体量子点；红外探测器；红外焦平面阵列；红外上转换器件

中图分类号 O436　　　**文献标志码** A　　　　　　　　　　　　　**DOI:** 10.3788/AOS230963

1 引　　言

红外探测器可远距离、全天候识别物体的光学信息，在卫星遥感、军事侦察等方面发挥了重要作用。目前红外探测器主要基于碲镉汞、铟镓砷、锑化铟等块体半导体材料[1]，需要在晶格匹配的衬底上通过分子束外延法制备，并且需要经过铟柱沉积、倒装键合等多项复杂工艺实现与读出电路的信号耦合[2]，导致了高昂的成本和较低的产率。然而，随着近年来半导体行业智能化、信息化及自动驾驶、智慧城市等领域的快速发展，在维持红外探测器高性能的前提下，降低器件成本、减小器件尺寸，实现大阵列规模、大批量晶圆级别制备逐渐成为了红外领域的研究热点。

胶体量子点（CQD）的出现为低成本、大规模、高分辨、小像元的红外探测器提供了新的发展思路[3]。胶体量子点是三维方向上电子限域的纳米半导体晶体，其典型尺寸在 1～20 nm 范围内。由于"量子限域效应"，量子点带隙可由有限高三维势阱模型描述，其能级可以通过量子点尺寸精准调控，进而实现宽光谱光响应。此外，胶体量子点可通过液相化学合成方法低成本大批量制备。液相加工工艺使得其可以与硅基读出电路进行直接片上耦合，突破了倒装键合工艺限制。过去的 15 年中，胶体量子点由于其光谱调控范围

宽、热注射法合成制备成本低、液相加工可直接涂覆在硅电子器件上的优势，在光电器件发展上取得了重大进展（图 1）。以碲化汞、硒化汞为代表的硫汞族半金属胶体量子点，具有波尔半径大、可调节尺寸范围大的优势，理论上可覆盖红外的各个主要波段，是红外探测器的理想材料。现有硫汞族胶体量子点合成技术已经实现热注射法合成不同尺寸量子点，光吸收谱截止波
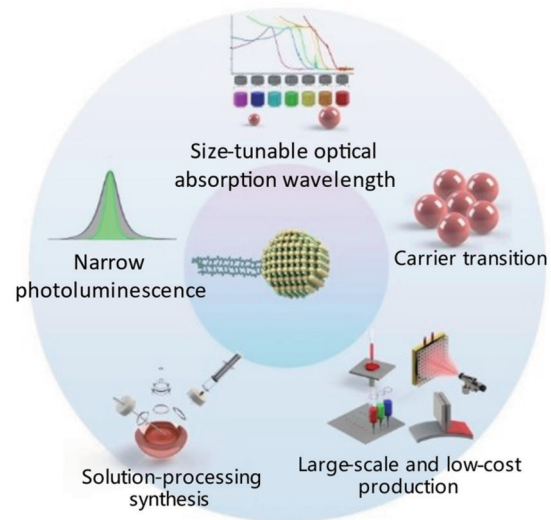

图 1　胶体量子点技术[4]
Fig. 1　Colloidal quantum dot technology[4]

长覆盖了短波、中波、长波红外等各个大气传输窗口[4]。

本文概括性地介绍了硫汞族胶体量子点红外探测器的研究现状与进展、硫汞族胶体量子点焦平面阵列的设计方法,并对硫汞族胶体量子点在各类探测中的应用进行阐述,简要讨论了硫汞族胶体量子点红外上转换探测器的发展进程。最后,对硫汞族胶体量子点的未来发展方向进行了讨论与展望。

2 硫汞族胶体量子点单点型红外探测器

胶体量子点光吸收过程主要分为带间跃迁吸收及带内跃迁吸收两种。带间跃迁发生于量子点导带与价带之间。当入射光能量大于或等于带间带隙时,入射光子能量可激发导带内电子跃迁,形成光吸收进而产生光生载流子。带内跃迁发生于导带或价带内,只有当入射光子能量等于带间带隙时,光子能量才可被吸收,进而形成载流子。

根据 k. p 微扰理论,胶体量子点带间带隙 E_{inter} 可表示为

$$E_{\text{inter}} = \frac{E_{\text{G}}}{2} + \sqrt{\frac{E_{\text{G}}^2}{4} + \frac{2}{3}E_{\text{p}}\frac{\hbar^2 k^2}{2m_0}} \ , \qquad (1)$$

式中:E_{G} 为体材料带隙;E_{p} 为 Kane 能量;$\hbar$ 为简化普朗克常数;m_0 为电子等效质量。与带间跃迁不同,带内跃迁型量子点带内带隙 E_{intra} 可表示为

$$E_{\text{intra}} = \sqrt{\frac{E_{\text{G}}^2}{4} + \frac{2}{3}E_{\text{p}}\frac{\hbar^2 k_{1p}^2}{2m_0}} - \sqrt{\frac{E_{\text{G}}^2}{4} + \frac{2}{3}E_{\text{p}}\frac{\hbar^2 k_{1s}^2}{2m_0}} \ , (2)$$

式中:k_{1p} 及 k_{1s} 为量子点 p 轨道及 s 轨道 k 值。带内跃迁的实现依赖于对量子点掺杂浓度及费米能级的精确调控。带内跃迁型量子点优势之一为可以突破小带隙材料的限制,开发基于宽带隙材料如金属氧化物(氧化镉、氧化钛、氧化铜、氧化锌等)的量子点体系。

2.1 硫汞族胶体量子点带间跃迁红外探测器

硫汞族胶体量子点红外光电探测器主要包括三类:光导型、光晶体管和光伏型。光导型探测器结构简单,可以通过在叉指电极上沉积胶体量子点来制备[5]。尽管制备方便,但是光导型器件存在暗电流及噪声大等问题。与光导型器件相比,光伏型器件在理论上可以避免 $1/f$ 噪声和暗电流,可以大大提高器件的灵敏度[6]。

硫汞族胶体量子点早期研究起源于美国芝加哥大学 Guyot-Sionnest 教授团队[7-20]。2011 年美国芝加哥大学团队报道了首个碲化汞胶体量子点中波红外光电探测器,基于带间跃迁过程,器件响应波段范围可覆盖 1.7~5 μm,比探测率达到 10^9 Jones(1 Jones=1 cm·Hz$^{-1/2}$·W^{-1})[7]。2015 年,该团队基于碲化银掺杂方法,开发了第一个达到背景限红外探测性能的量子点探测器[16],比探测率达到 4.2×10^{10} Jones,响应时间在 μs 级别,器件结构如图 2(a)所示。2018 年,该团队通过氯化汞激活的碲化银掺杂方法进一步提高了光电
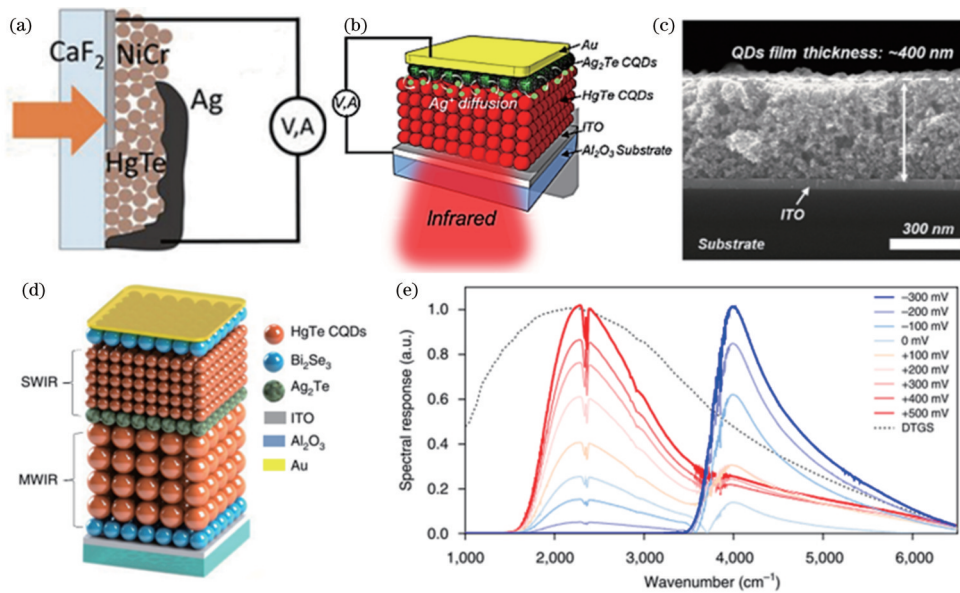

图 2 美国芝加哥大学在硫汞族胶体量子点带间跃迁红外探测器方面的研究。(a)器件结构示意图[16];(b)探测器结构示意图[21];(c)所制备的探测器的横断面扫描电子显微镜[21];(d)双波段胶体量子点探测器的结构示意图,在氧化铟锡(ITO)和金触点(接地)之间施加偏置电压[22];(e)在 85 K 的正(+500 mV)到负(−300 mV)偏置电压下,双波段探测器的光谱响应[22]

Fig. 2 Interband transition infrared detectors based on mercury chalcogenide CQDs by the University of Chicago. (a) Schematic of the device structure[16]; (b) schematic of the detector structure[21]; (c) cross-sectional scanning electron microscope of the fabricated detector[21]; (d) illustration of the structure of a dual-band CQD imaging device, bias voltage is applied between the indium tin oxide (ITO) and the Au contact (grounded)[22]; (e) spectral response of the dual-band detector under a bias voltage from positive (+500 mV) to negative (−300 mV) voltage at 85 K[22]

探测器的灵敏度和响应速度[21]，如图 2(b)、(c)所示。2019 年，在前期单波段探测器研究及掺杂工艺基础之上，通过使用垂直堆叠的胶体量子点光电二极管结构，该团队实现了双波段短波红外及中波红外探测器的制备，在两个不同的波段提供了可偏置切换的光谱响应，如图 2(d)[22]所示。双波段器件由一个短波和一个中波红外光电二极管组成，以 n-p-n 背靠背结构排列，硒化铋和碲化银分别作为 n 层和 p 层。通过控制偏置极性和幅度，它可以在调制频率高达 100 kHz 的短波和中波红外之间快速切换[图 2(e)]，比探测率在低温下高于 10^{10} Jones。

为满足解决量子点红外探测器批量化制备需求，突破传统外延红外材料产量及成膜均匀性瓶颈，2020年，北京理工大学光电学院郝群、唐鑫及陈梦璐团队首先提出并实现了一种高效的掩模式喷涂光刻技术。胶体量子点在成膜过程中，量子点位置、间距可沿应力最小方向重排，解决传统外延材料晶格失配及应力失调难题，可以在 4 英寸(1 英寸＝2.54 cm)刚性、柔性和弯曲的基底之上沉积厚度均匀、表面光滑的胶体量子点薄膜[图 3(a)、(b)][23]。所制备的六通道的柔性多光谱碲化汞胶体量子点探测器，可在光导型和光伏型模式下运行，且覆盖短波和中波红外响应波段，其峰值比探测率高于 10^{11} Jones，并且其噪声等效温差低至 26.7 mK。通过所提出的喷涂光刻方法可以对不同的光谱范围做出响应，实现宽光谱多波段探测[图 3(c)]。

以此为基础，北京理工大学团队先后在可见光-短波红外双波段探测、短波红外-中波红外双模式探测及光学谐振增强的双色红外探测方面实现突破。从单一波段到多波段探测的提升依赖于能带结构精准设计及实现。首先，该团队通过探索背靠背双光电二极管结构，提出了一种基于硫族胶体量子点(碲化汞和碲化镉胶体量子点)的双波段可见光和短波红外探测器[24]。通过在碲化镉和碲化汞层之间引入了 n 型氧化锌层作为电子传输层和空穴阻挡层，防止来自不同传感层的空穴注入，使探测器能够通过改变偏置电压的极性和大小在可见光和短波红外模式之间切换，且比探测率高于 10^{11} Jones，如图 3(d)~(f)所示。
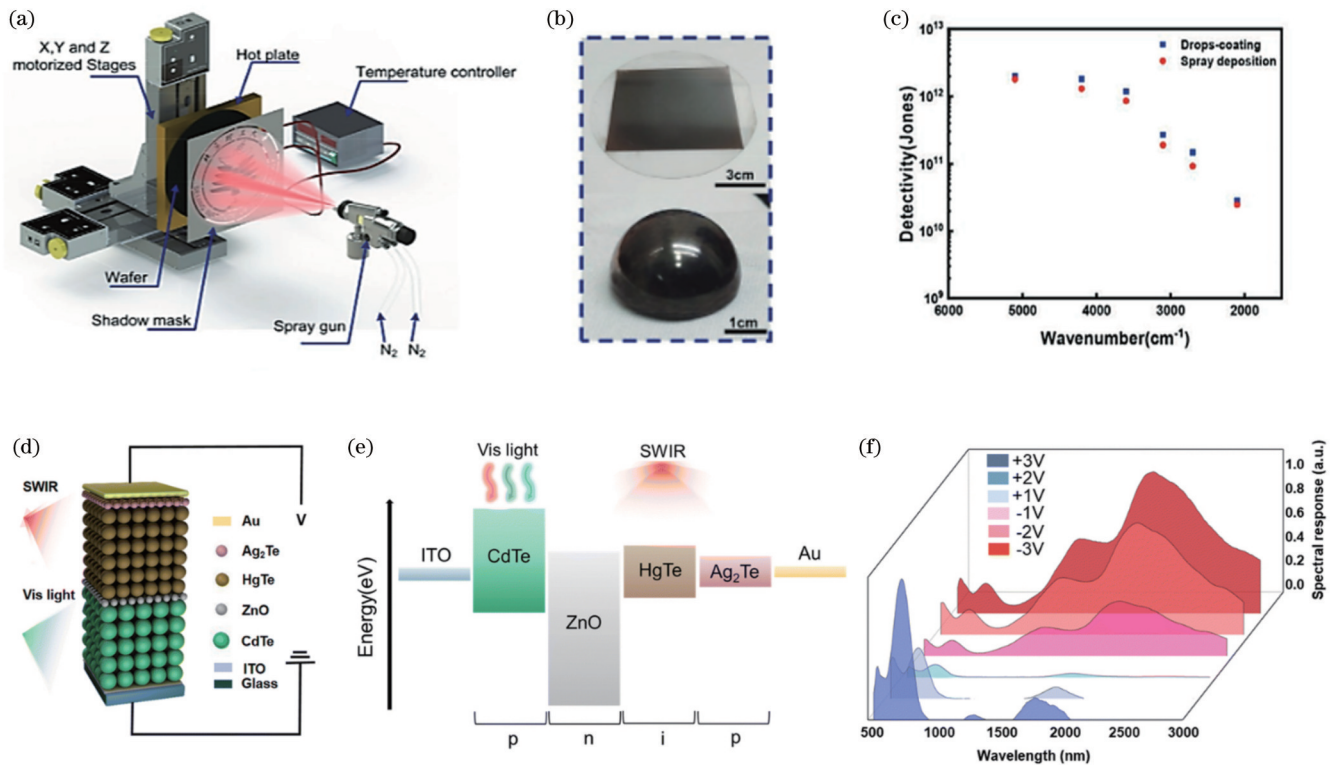

图 3 北京理工大学在硫汞族胶体量子点带间跃迁红外探测器方面的研究。(a)掩模式喷涂光刻技术示意图[23]；(b)胶体量子点薄膜在 4 英寸基片和玻璃半球上的照片[23]；(c)掩模式喷涂光刻技术和滴涂法制备的探测器的比探测率比较[23]；(d)双波段器件结构图[24]；(e)双波段器件的能带结构图[24]；(f)双波段器件在正偏置和负偏置下的响应谱[24]

Fig. 3   Interband transition infrared detectors based on mercury chalcogenide CQDs by Beijing Institute of Technology. (a) Schematic of spray-stencil lithography platform[23]; (b) photograph of CQD films on a 4 inch substrate and a glass hemisphere[23]; (c) detectivity as a function of wavenumber of detectors fabricated by spray-stencil lithography and drop-coated[23]; (d) structure diagram of the dual-band device[24]; (e) energy band structure diagram of the dual-band device[24]; (f) response spectra of the dual-band device under positive and negative bias[24]

2022年,北京理工大学团队进一步提出了一种胶体量子点双模式能带设计及叠层探测器结构,能够探测、分离和融合来自不同波长范围的光子[图 4(a)][25]。利用三个垂直堆叠的胶体量子点同质结,通过控制偏置极性和大小,在同一个探测器上可以实现单波段短波红外成像和融合波段成像[图 4(b)、(c)]。双模式探测器的探测率分别达到融合波段模式 8×10^{10} Jones 和单波段模式 3.1×10^{11} Jones。双波段探测

器的出现为光学结构设计提出了更高要求,传统光学增强方法如等离子共振、光子晶体、超材料等大多针对单一波段,为实现双/多波段探测器的性能提升,该团队创新性地提出了一种胶体量子点双波段红外光电探测器法布里-珀罗谐振腔的设计及集成方式[26],可以同时针对短波和中波红外提供光吸收增强[图 4(d)]。同时,由于谐振腔的存在,探测器的性能可以通过提高光学收集效率和光谱选择性而得到提升。该双波段探
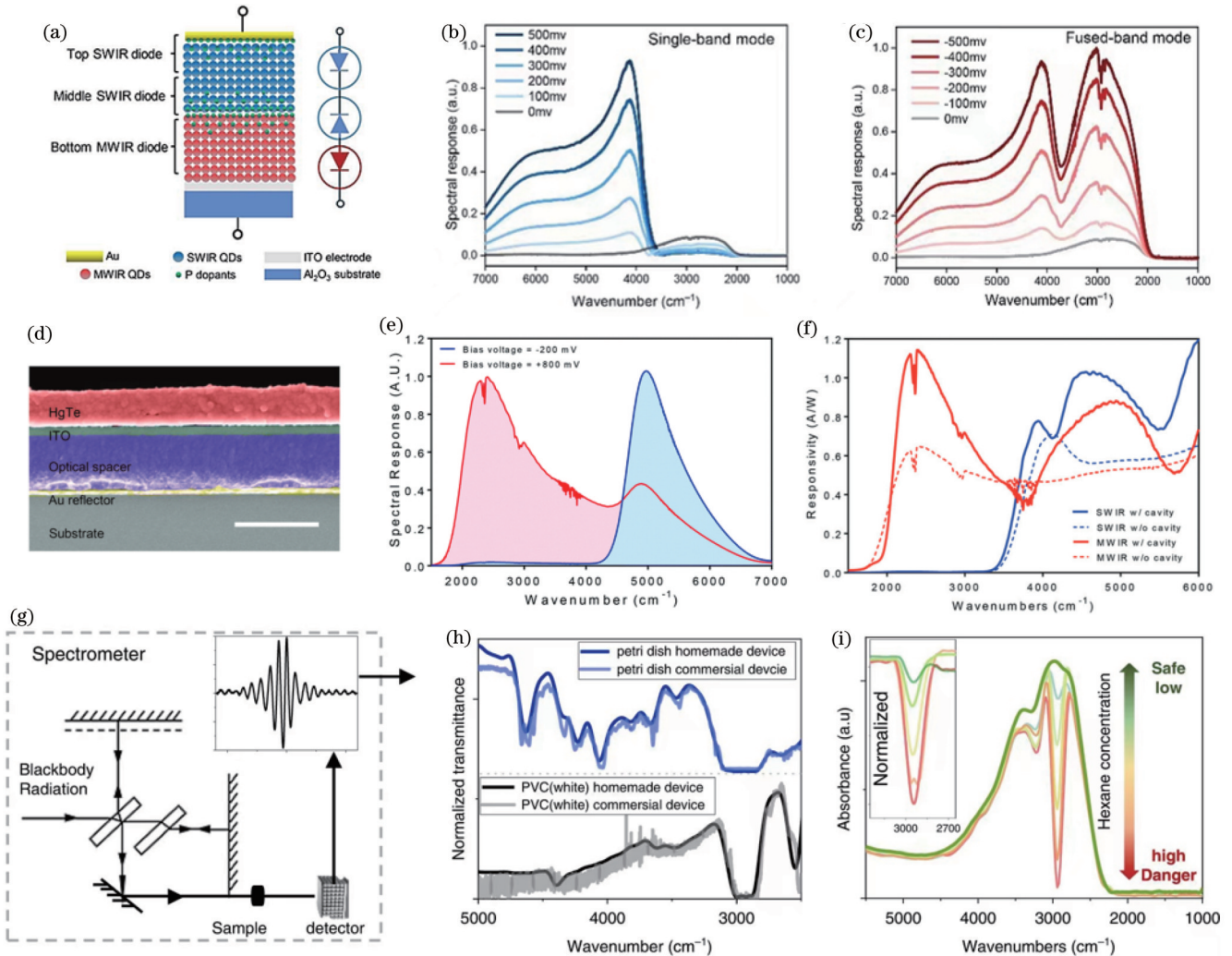

图 4 北京理工大学在硫汞族胶体量子点带间跃迁红外探测器方面的研究。(a)胶体量子点双波段红外光电探测器的结构图(插图:双波段红外光电二极管的等效电路)[25];(b)正偏置电压和(c)负偏置电压下的偏置相关频谱响应[25];(d)具有谐振腔的双波段光电探测器的横断面扫描电子显微镜图像(比例尺:1 μm)[26];(e)具有谐振腔的双波段探测器在 80 K 时正(+800 mV)和负(−200 mV)偏置电压下的光谱响应[26];(f)在 80 K 时,有谐振腔和没有谐振腔的短波红外/中波红外模式的光谱响应率[26];(g)常温中红外光电探测器光谱响应装置的光谱仪示意图[27];(h)通过同质结探测器和傅里叶变换光谱仪测量的透射率[27];(i)空气中不同己烷浓度的吸收[27]

Fig. 4 Interband transition infrared detectors based on mercury chalcogenide CQDs by Beijing Institute of Technology. (a) Illustration of dual-mode colloidal quantum-dot photodetector (inset: equivalent circuit of dual band infrared photodiode)[25]; bias-dependent spectral response under (b) positive and (c) negative bias voltages[25]; (d) cross-sectional scanning electron microscopy image of the dual-band photodetector (scale bar: 1 μm)[26]; (e) spectral response of the dual-band detector under a positive (+800 mV) and negative (−200 mV) bias voltage at 80 K[26]; (f) spectral responsivity of the short-wave infrared /mid-wave infrared mode with and without the cavity at 80 K[26]; (g) schematic diagram of the spectrometer with a homojunction device[27]; (h) transmission measured by homojunction device and Fourier transform spectrometers[27]; (i) absorption with different hexane concentrations in the air[27]

测器在短波和中波红外中的响应率分别为 $1.1 \text{ A} \cdot \text{W}^{-1}$ 和 $1.6 \text{ A} \cdot \text{W}^{-1}$，增强率约 200%～300%[图 4（e）～（f）]。在高温运行方面，该团队利用高迁移率胶体量子点研究了一个具有量子点梯度同质结的常温中红外光电探测器[27]。该探测器在 80 K 时在 4.2 μm 上实现了背景限制性能，比探测率达到 2.7×10^{11} Jones，在 200 K 前高于 10^{11} Jones，在 280 K 前高于 10^{10} Jones，在 300 K、3.5 μm 截止波长上达到 7.6×10^{9} Jones。光谱

仪、化学传感器和热像仪等应用也得到了验证，如图 4（g）～（i）所示。

2.2 硫汞族胶体量子点带内跃迁红外探测器

与碲化汞宽光谱吸收与探测不同，硒化汞量子点由于采用带内跃迁吸收方式，可以实现窄带光响应。2014 年，美国芝加哥大学团队首次开发了基于硒化汞胶体量子点的带内跃迁型红外探测器[图 5（a）][28]。探测器带内吸收峰约为 2000～3000 cm^{-1}，覆盖中波红
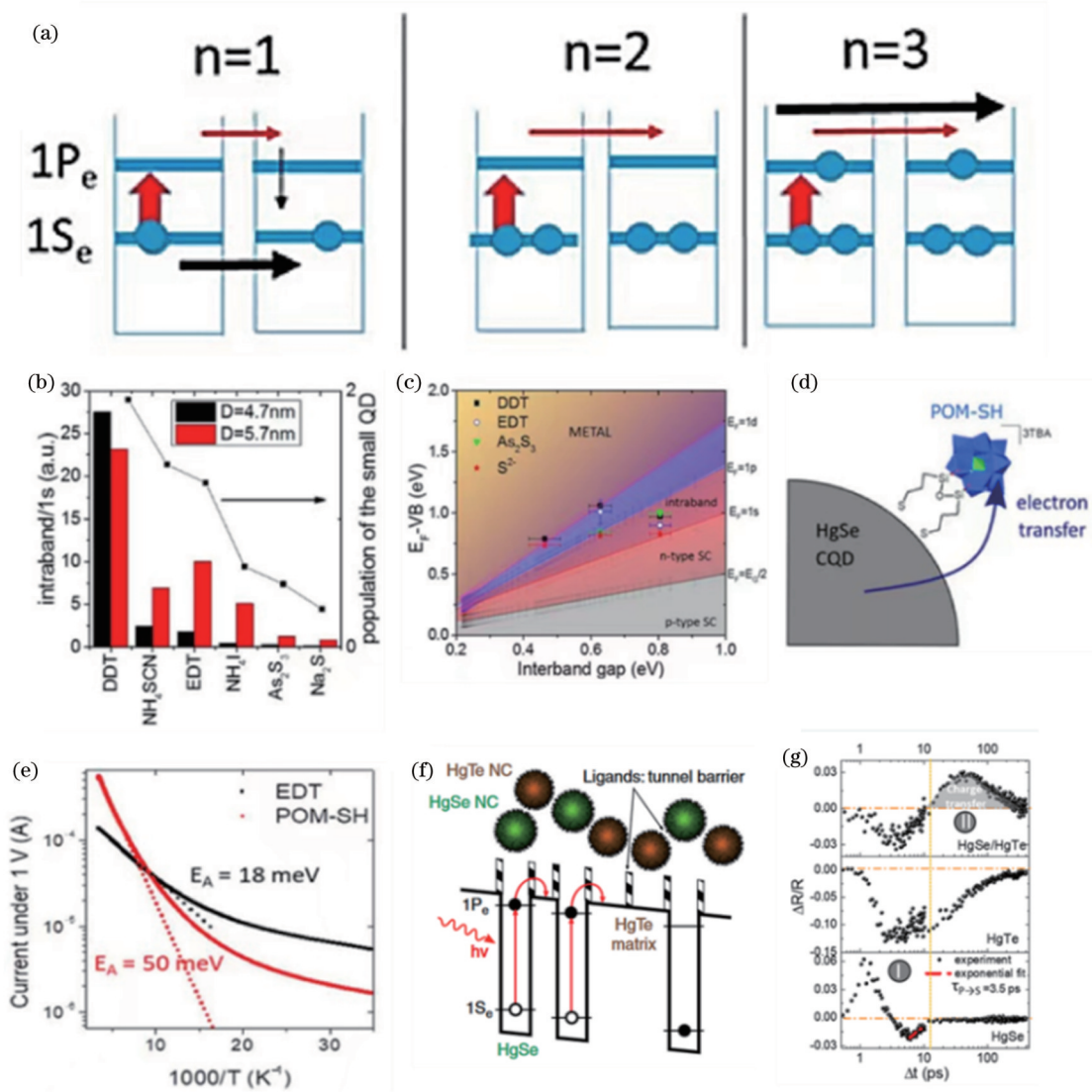

图 5　代表性团队在硫汞族胶体量子点带内跃迁红外探测器方面的研究。(a)带内传导中掺杂电子的示意图[28]；(b)对于两种尺寸的纳米晶体，带内信号除以 1 s 带间信号拟合幅度的比值图[31]；(c)费米能级与价带的关系是带间隙的函数[32]；(d)具有 POM-SH 配体的硒化汞胶体量子点示意图[33]；(e)电流与温度的关系，$V_{DS}=1 \text{ V}$[33]；(f)以硒化汞纳米晶体为吸收材料，碲化汞纳米晶体为阻挡材料的胶体量子点红外探测器偏振带结构示意图[34]；(g)由硒化汞（下）、碲化汞（中）和硒化汞/碲化汞混合物（上）组成的薄膜的瞬态反射率信号随时间的变化[35]

Fig. 5　Intraband transition infrared detectors based on mercury chalcogenide CQDs by representative groups. (a) Doping requirement for intraband conduction[28]; (b) plot of the ratio of the intraband signal divided by the fitted magnitude of 1 s interband signal for two sizes of nanocrystals[31]; (c) Fermi energy with respect to the valence band as a function of the interband gap[32]; (d) scheme of HgSe QDs capped with POM-SH ligands[33]; (e) current as a function of decreasing temperature, $V_{DS} = 1 \text{ V}$[33]; (f) scheme of polarized band structure of a random colloidal quantum dot infrared photodetector consisting of HgSe nanocrystals as absorber material and HgTe nanocrystals as barrier material[34]; (g) transient reflectivity signal as a function of time for the film made of HgSe (bottom), HgTe (middle), and HgSe/HgTe mixture (top)[35]

外范围,最大的响应度为 1.2×10^{-2} A·W^{-1}。通过掺杂调控,可使导带被两个电子充满,获得最小暗电流,随着器件工作温度从 300 K 冷却到 80 K,暗电流可以减少为 1/3200,在 80 K 时比探测率达到 8.5×10^8 Jones。同年,该团队证实了强约束胶体量子点的量子态中存在稳定的载流子并实现了带内光致发光[29]。2016 年,芝加哥大学团队研究了空气稳定的 n 型掺杂硫化汞胶体量子点和硫化汞/硫化镉胶体量子点的带内转换[30]。此种核/壳结构改善了硫化汞核的热稳定性,对硫化汞胶体量子点材料的研究拓展了硫汞族材料在带内转换中的应用。

2016 年,法国索邦大学团队探索了配体修饰对硒化汞胶体量子点性能的影响,实现了每量子点 0.1~2 个电子之间的精确掺杂调控[图 5(b)][31]。2017 年,该团队测量了不同配体交换的硒化汞胶体量子点的绝对能量水平[图 5(c)][32],并提出了一种将功能化的聚氧乙烯(POM)嫁接到硒化汞胶体量子点表面的方法,降低了暗电流同时增加器件激活能[图 5(d)、(e)][33]。2019 年,该团队提出了碲化汞和硒化汞胶体量子点混合物,并将材料集成到光电二极管中[图 5(f)][34]。在 80 K 时,比探测率可以达到 1.5×10^9 Jones,在相同温度和波长下,相比于单一硒化汞量子点探测器高 2 倍。2022 年,该团队通过使用中红外瞬态反射率测量方法揭开了硒化汞和碲化汞材料之间的耦合关系[图 5(g)][35]。这种硒化汞和碲化汞耦合的叠层结构保留了硒化汞的带内吸收,减少了暗电流,并缩短了响应时间。这种叠层材料结构被耦合到一个导引模式谐振腔上,使得来自带内跃迁的光电流信号增强了 4 倍。在 80 K 和 5 μm 时,比探测率达到 10^9 Jones,响应率达到 3 mA·W^{-1}。

2020 年,北京理工大学团队提出了一种混合配体交换方法生产高迁移率的硒化汞胶体量子点薄膜,并与乙二硫醇的固态配体交换进行了比较[36]。在直径为 7.5 nm 的量子点中,其迁移率达到了 1 cm^2/(V·s),与硒化汞/乙二硫醇薄膜相比,迁移率增加了 100 倍[图 6(a)~(c)]。随后,该团队研究了硒化汞胶体量子点的尺寸分布对迁移率、导电间隙和带内光传导的影响[37]。结果显示,迁移率与尺寸分布呈指数关系,而带内光导特性可以通过改善尺寸分布得到增强[图 6(d)~(f)]。基于硒化汞量子点探测器,该团队开发了一种高性能的带内热成像相机以及二氧化碳气体传感器[图 6(g)],其范围为 $(0.25 \sim 2000) \times 10^{-6}$,灵敏度为 0.25×10^{-6},响应速度达到了几微秒,响应度为 77 mA·W^{-1}[38]。与低迁移率硒化汞量子点探测器相比,响应速度及响应度提升 1000 倍及 55 倍。在 80 K 时,比探测率达到了 1.7×10^9 Jones,与低迁移率器件相比,性能高出一个数量级以上。图 6(h)显示了基于硒化汞胶体量子点带内跃迁探测器的热成像。为了进一步提高基于硒化汞胶体量子点的带内跃迁探测器的性能,除能带结构设计之外,香港城市大学团队设计了一个基于硒化汞胶体量子点薄膜的金纳米盘阵列,并通过等离子体共振增强了光响应[图 6(i)][39]。四个波段(4.2 μm、6.4 μm、7.2 μm 和 9.0 μm)的探测器被集成到等离子体纳米盘阵列。如图 6(j)所示,响应速度分别达到 145 mA·W^{-1}、92.3 mA·W^{-1}、88.6 mA·W^{-1} 和 86 mA·W^{-1}。

2.3　硫汞族胶体量子点红外上转换器件

红外-可见光上转换器件通过集成探测红外光子的红外探测器和激发可见光子的发光二极管,利用器件内部光-电-光的线性转换过程,避免了读出电路和复杂的电信号处理过程,能够直接可视化红外图像[图 7(a)]。其具有很多优点:1)无需通过繁琐的读出电路传输电信号,利用肉眼或可见光相机直接观察红外图像,突破了传统红外成像分辨率的限制,显著提升了红外成像的分辨率;2)无需复杂的信号采集、放大及处理过程,实现了实时红外上转换成像,显著提高了红外成像的帧频和灵敏度;3)无需通过复杂的倒装键合工艺互连铟柱并对准每个像素,极大简化了工艺过程,显著降低了成像成本。尽管红外-可见光上转换成像技术得到了广泛关注,针对低成本、宽光谱、高分辨率、高灵敏度红外上转换成像的研究,目前仍存在以下诸多难点。首先,现有上转换器件受限于材料体系能带带隙限制,红外探测波段范围主要局限于近红外波段,很难拓展至短波、中波,甚至长波等重要的红外波段,极大地限制了红外上转换器件应用范围[40-46]。并且,目前上转换器件红外探测单元和可见光发光单元只是简单堆叠,上转换器件灵敏度较差,只能探测激光强度的红外光,无法探测到自然界中微弱的红外,致使应用范围严重受限[40,44,47-48]。

基于以上挑战,2022 年北京理工大学团队开发了基于胶体量子点的红外-可见光上转换器件,该器件使用碲化汞胶体量子点作为红外光敏层,硒化镉/硫化锌胶体量子点作为可见光发光层[图 7(b)],首次拓宽了红外上转换器件的探测波段范围到 2.5 μm 短波红外,实现了短波红外到可见绿光的上转换[图 7(c)][49]。研究人员发现发光单元亮度灵敏度在特定偏压范围内达到最大,传统上转换器件只是探测单元和发光单元的简单堆叠,使得发光单元工作电压区间无法处于最优范围,致使上转换器件灵敏度较差[图 7(d)]。基于此,研究人员建立了红外上转换理论模型,通过模型结果确定与发光单元最优匹配的红外探测单元电阻特性,并设计优化红外探测单元结构,使得集成后的上转换器件的发光单元处于最优工作偏压区间,从而使上转换器件的灵敏度和上转换效率最大化[图 7(d)]。最优匹配红外探测单元和发光单元集成的上转换器件具有超高的灵敏度,能够探测红外功率低至 20 μW·cm^{-2},如图 7(e)所示。并且,此上转换器件具有接近 30% 的超高上转换效率,如图 7(f)所示,此上转换器件的性能达到目前领先水
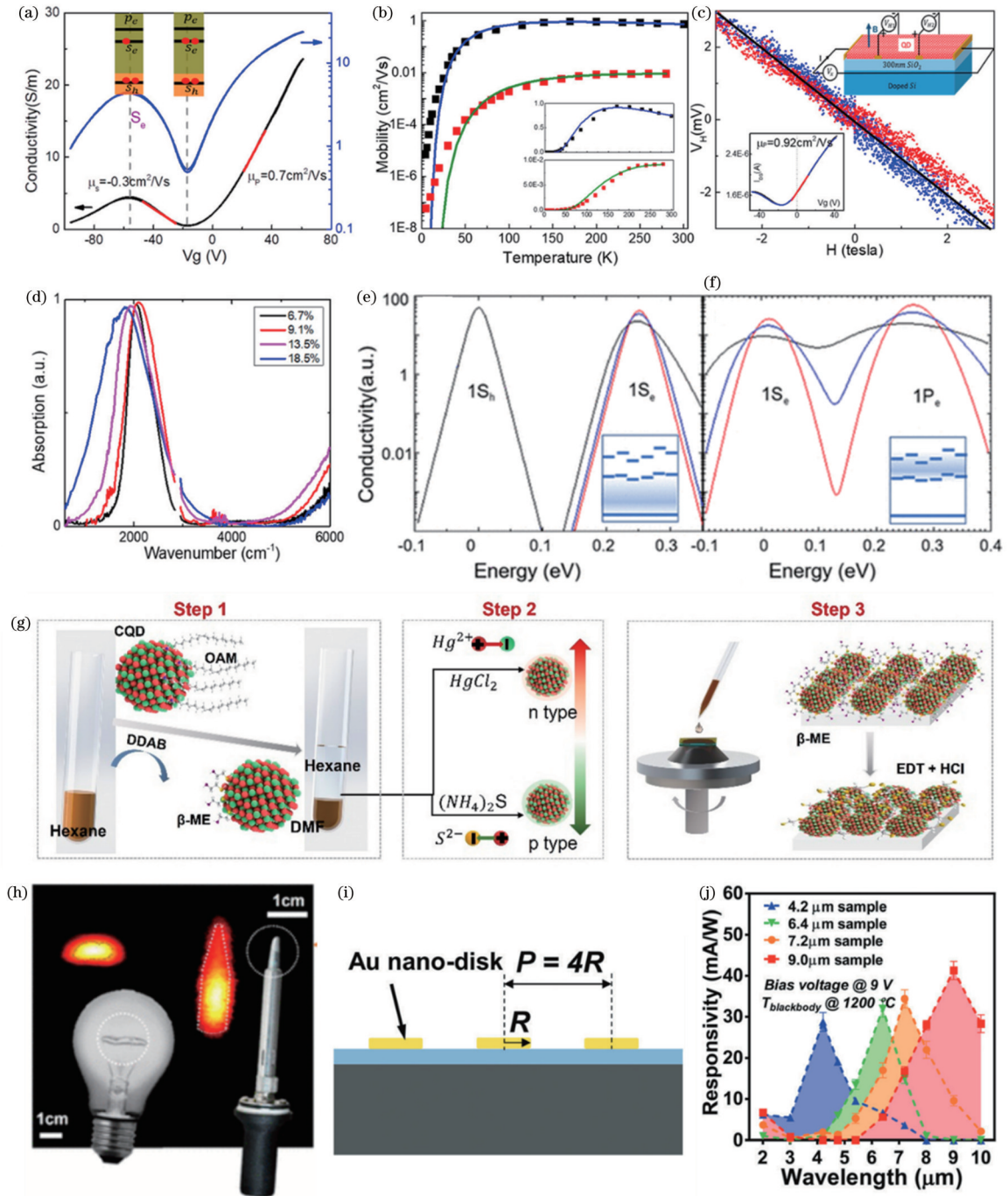
图 6　北京理工大学在硫汞族胶体量子点带内跃迁红外探测器方面的研究。(a)硒化汞胶体量子点使用混合配体交换在 80 K 时的场效应晶体管源-漏电流[36]；(b)硒化汞胶体量子点使用混合配体交换(黑色)和硒化汞胶体量子点使用固态配体交换(红色)场效应晶体管迁移率随温度的函数以及 Marcus 理论拟合结果[36]；(c)直径为(7.5±0.5)nm、厚度为(35±5)nm 的硒化汞胶体量子点使用混合配体交换制备的薄膜在 200 K 时测量的霍尔电压[36]；(d)不同尺寸分布硒化汞/固相配体交换薄膜的 1Se－1Pe 激子谱[37]；(e)(f)80 K 时 0.25 eV 带间带内间隙的尺寸分布效应[37]；(g)混相配体交换过程示意图[38]；(h)硒化汞带内光电探测器红外热成像[38]；(i)二氧化硅/硅上等离子体磁盘阵列的原理图[39]；(j)4.2 μm 样品、6.4 μm 样品、7.2 μm 样品和 9.0 μm 样品的光谱响应率[39]

Fig. 6　Intraband transition infrared detectors based on mercury chalcogenide CQDs by Beijing Institute of Technology. (a) Field effect transistor source-drain current for HgSe/Hybrid at 80 K[36]; (b) field effect transistor mobility of HgSe/hybrid (black) and HgSe/EDT (red) as a function of temperature as well as Marcus theory fitting[36]; (c) Hall voltage measured at 200 K of (7.5±0.5) nm diameter HgSe/Hybrid QD film with thickness (35±5) nm[36]; (d) 1Se － 1Pe exciton spectra of films of HgSe/EDT with different size distributions[37]; (e)(f) size distribution effect on 0.25 eV interband and intraband gaps at 80 K[37]; (g) schematic diagram of the mixed-phase ligand exchange process[38]; (h) infrared hot images by a HgSe intraband CQD photodetector[38]; (i) schematic of plasmonic disk arrays on SiO₂ /Si[39]; (j) spectral responsivity of 4.2 μm samples, 6.4 μm samples, 7.2 μm samples, and 9.0 μm samples[39]

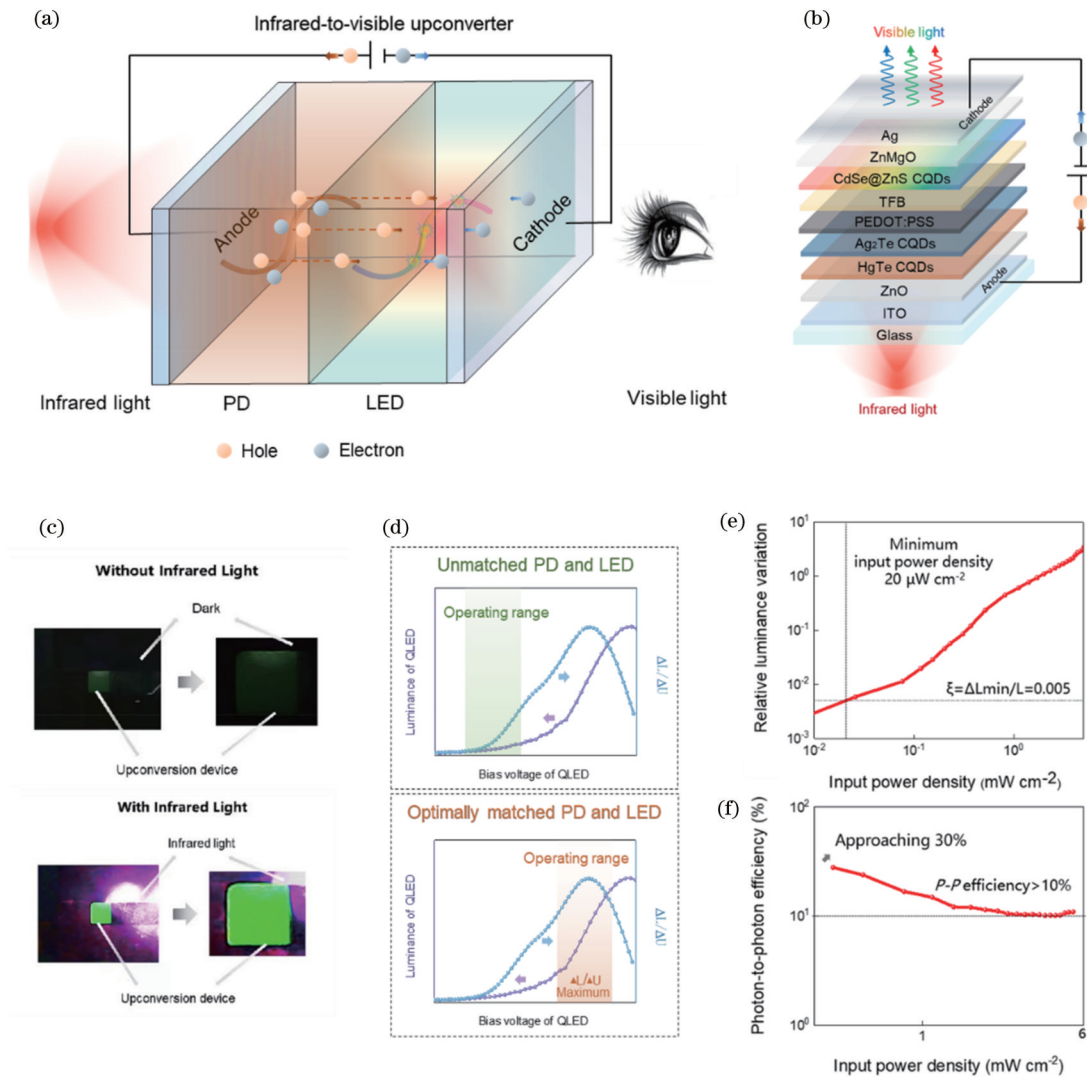平。该研究表明,取代传统有机/无机材料的胶体量子点材料以及红外探测单元和发光二极单元的优化

匹配方式为上转换技术中长期存在的挑战提供了潜在的解决方案。

图 7　北京理工大学在碲化汞胶体量子点红外-可见光上转换器件方面的研究[49]。(a)红外-可见光上转换器件工作原理示意图;(b)红外-可见光上变换器件结构示意图;(c)无红外和有红外下上转换器件照片;(d)未匹配的光电探测单元与发光单元耦合的和最佳匹配的光电探测单元与发光单元耦合的上转换器件的比较;(e)在 16 V 电压下,上转换器件的相对亮度随红外功率密度的变化情况;(f)上转换器件的红外-可见光上转换效率随红外功率密度的变化情况

Fig. 7　HgTe CQDs-based infrared-to-visible upconverters by Beijing Institute of Technology[49]. (a) Operational mechanism of infrared-to-visible upconverters; (b) architecture schematic of infrared-to-visible upconverter; (c) images of an upconversion device without and with infrared light; (d) comparison between unmatched photodetector with light-emitting diode-coupled and optimally matched photodetector with light-emitting diode -coupled upconverters; (e) relative luminance variation with the dark condition of upconverters varying with infrared power densities at the applied voltage of 16 V; (f) infrared-to-visible upconversion efficiency of upconversion devices varying with infrared power densities

3　硫汞族胶体量子点红外焦平面阵列

　　胶体量子点相比传统红外块体半导体在加工工艺方面具有显著优势,可以通过滴涂或旋涂方式在硅基读出电路上制备红外探测器,不需要晶格匹配的分子束外延过程及复杂的倒装键合工艺,大大降低了红外焦平面阵列探测器的制备成本。2016 年,美国芝加哥大学研究团队报道了第一个胶体量子点焦平面阵列红外探测器,通过将碲化汞胶体量子点与硅基电路耦合,

在低温下实现了中波红外成像,如图 8(a)～(c)所示[50]。在 95 K 时,量子效率、比探测率和噪声等效温差(NETD)分别为 0.30%、1.46×10⁹ Jones 和 2.319 K。在 5 μm 处其噪声等效差为 1.02 K,帧频达到了 120 frame/s[51]。胶体量子点薄膜中的缺陷会大大降低探测器的性能。因此,优化胶体量子点制膜工艺是提高探测器性能的关键技术。2022 年法国索邦大学研究团队通过旋涂技术路线制备了光导型碲化汞胶体量子点焦平面阵列,阵列规模 640×512,像元尺寸 15 μm

[图 8(d)][52]。碲化汞胶体量子点焦平面外量子效率（EQE）为 4%～5%，使用帕尔蒂尔冷却，其截止波长为 1.8 μm。在图 8(e)、(f)中，一个 ITO 覆盖的玻璃和一个硅片被放置在不同的试剂瓶前面。在可见光及短波红外波段，由于 ITO 玻璃、化学试剂以及硅片截止波长的不同，拍摄图片呈现出截然不同的状态。
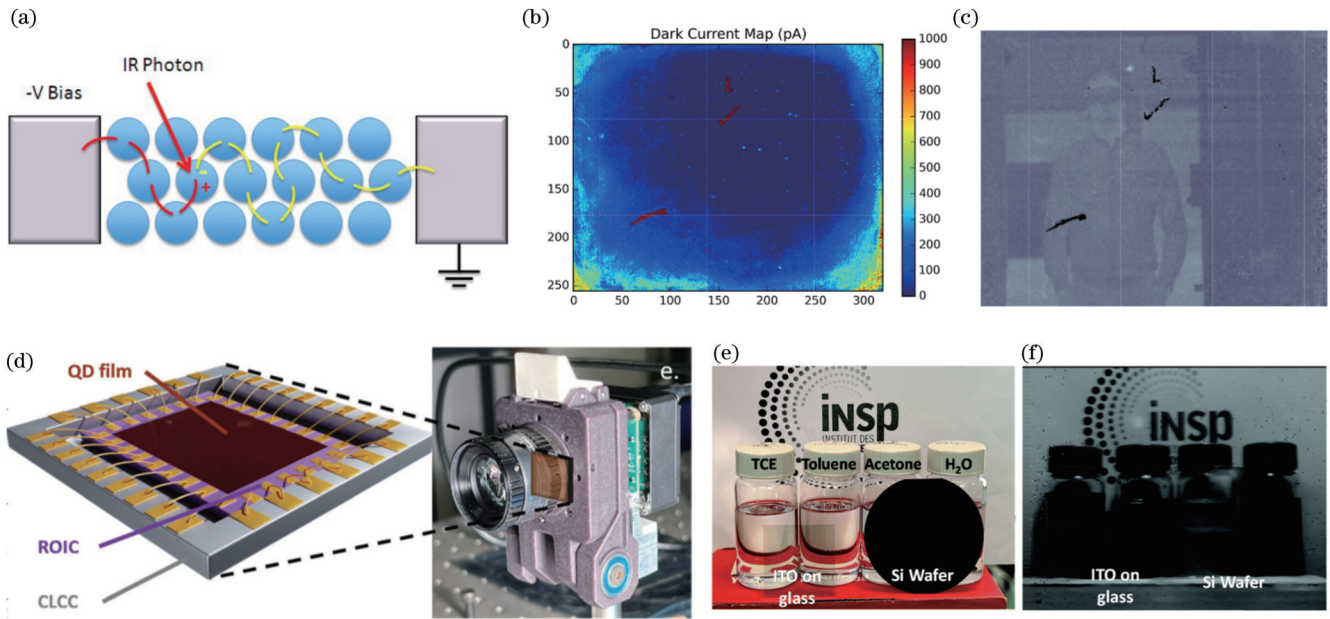

图 8　硫汞族胶体量子点红外焦平面阵列研究。(a)胶体量子点焦平面阵列光导型示意图[50]；(b)320×256中波红外胶体量子点焦平面阵列的暗电流图[50]；(c)一个人在门口的中波红外图像[50]；(d)插入摄像机的碲化汞量子点薄膜示意图，短波红外相机与Computar M1614-SW 物镜的图片[52]；(e)一个场景的可见光图片（智能手机摄像头），四个小瓶从左到右分别装有四氯乙烯、甲苯、丙酮和水，在小瓶的前面放置一个 ITO 覆盖的玻璃片和一个 2 英寸的硅片[52]；(f)使用碲化汞量子点焦平面阵列拍摄的与图(e)中相同的场景的红外图片[52]

Fig. 8　Study on infrared focal plane array based on mercury chalcogenide CQDs. (a) Diagram of photoconduction in a CQD detector[50]; (b) map of the dark current for the 320×256 mid-wave infrared CQDs focal plane array[50]; (c) mid-wave infrared image of a person in a doorway[50]; (d) scheme of the device that is plugged in the camera based on a film of HgTe CQDs, picture of the short-wave infrared camera with a Computar M1614-SW objective[52]; (e) visible picture (smartphone camera) of a scene with four vials containing tetrachloroethylene (TCE), toluene, acetone, and water (H₂O), and an ITO covered glass slide and a 2 inch silicon wafer are placed[52]; (f) same scene as in Fig. (e) taken with the HgTe QD based focal plane array[52]

2022 年，北京理工大学团队提出了一种与硅基读出电路完全兼容的捕获型光电探测器的设计。量子点与读出电路的耦合可以通过顺序旋涂工艺完成。与垂直光电二极管结构不同，捕获型光电探测器不需要额外的顶层电极，大大降低了读出电路成像器件的制造复杂性[图 9(a)、(b)]。为了获得最佳探测性能，采用了具有阻抗匹配的定制读出电路，在 8 英寸晶圆上进行晶圆级探测器制备[图 9(c)]。在此项工作中，团队系统研究了三种不同类型的成像芯片，包括光导型、光伏型和捕获型探测器。光导型量子点可以输出均匀的图像，但其探测效率有限，导致灵敏度低。尽管在原理上，光伏型成像芯片应该具有最高的灵敏度及较低的暗电流和高量子效率。然而，在实际制造过程中，典型光伏碲化汞量子点成像器件受到掺杂剂不可控扩散的影响，导致性能下降。捕获型量子点成像芯片将外部电场和内部电场结合在一起，既具有高灵敏度，又能够实现较好的响应均匀性。无需高强度激光激发，使用黑体辐射源即可获得较高响应。捕获型成像芯片响应非均匀性约为 4%，外量子效率达到 175%，短波红外室温下比探测率约为 $2×10^{11}$ Jones，并完成了中波红外成像[图 9(d)][53]。

在单波段量子点焦平面阵列基础之上，该团队针对现有硅基互补金属氧化物半导体（CMOS）传感器探测光谱范围仅限于可见光（0.4～0.7 μm）和近红外（0.8～1.1 μm）的问题，通过对修饰在读出电路上的胶体量子点材料使用直接光刻工艺构建宽光谱 CMOS 兼容的跨波段紫外-红外量子点探测器，实现了从紫外到短波红外（300～2500 nm）的探测[图 10(a)]。通过此项研究能够使用单片成像芯片实现单色或多光谱合并的高分辨率图像获取[54]。图 10(b)～(d)为使用多谱段宽光谱量子点探测器对包含 580 ℃ 的电烙铁、硅片和紫外灯的场景进行成像，可以看到使用一个多谱段宽光谱量子点探测器模组便能够获取该场景下紫外、可见光、短波红外信息特征（电烙铁释放的能够穿透硅片的短波红外信息、紫外发光二极管释放的紫外光信息、线材和紫外发光二极管模组的可见光信息），通过
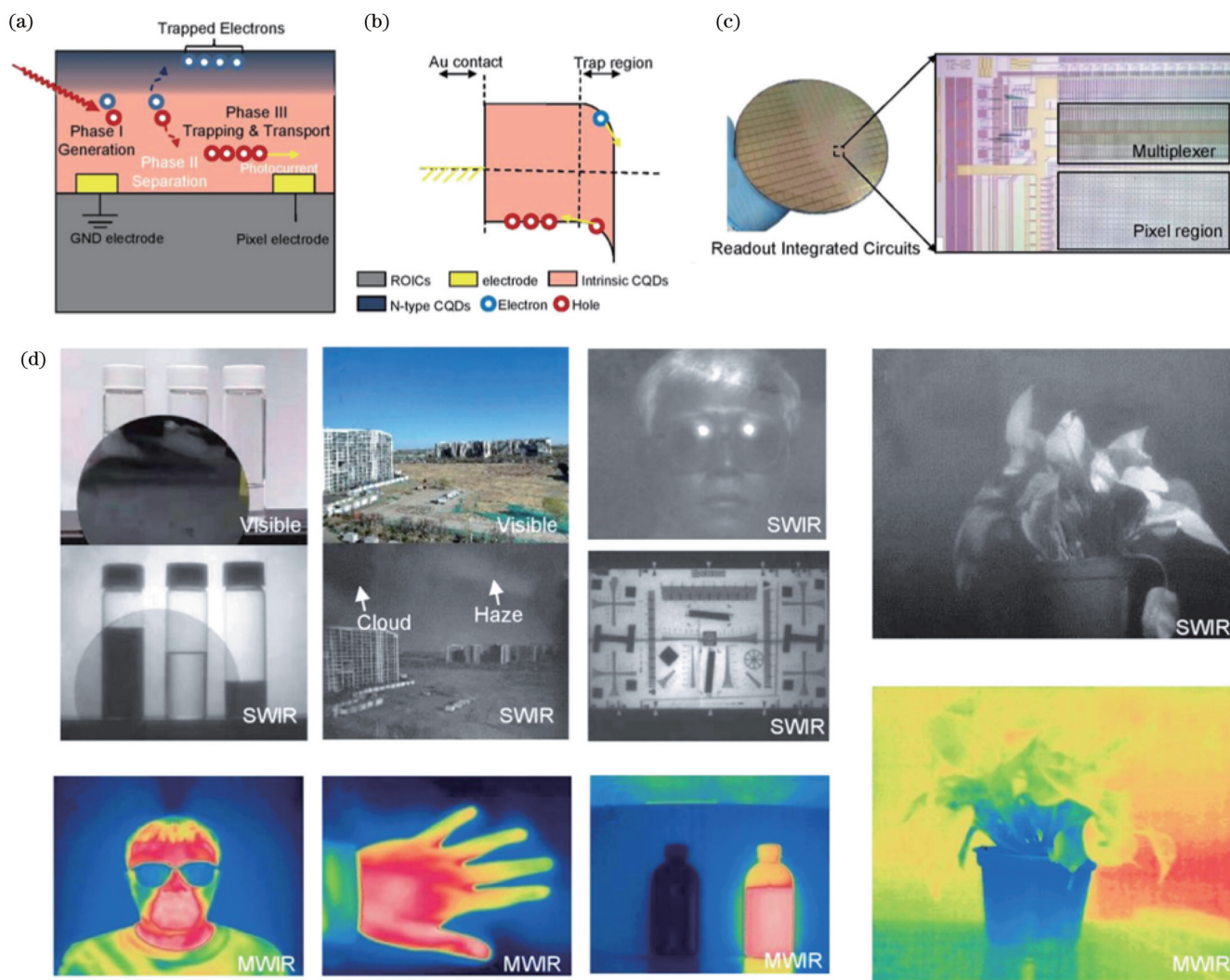
图 9 硫汞族胶体量子点红外焦平面阵列研究[53]。(a)捕获型光电探测器的工作原理示意图;(b)捕获型光电探测器的能带图;(c)8英寸晶圆制备和像素区域的放大视图;(d)捕获型成像仪获得的短波和中波红外图像

Fig. 9 Study on infrared focal plane array based on mercury chalcogenide CQDs[53]. (a) Illustration of the working process of trapping-mode photodetectors; (b) energy band diagrams of the trapping-mode photodetectors; (c) 8 inch silicon readout integrated circuit wafer and zoomed view of the pixel region; (d) captured short-wave and mid-wave infrared images with CQD imagers

图像的融合可以展现出从紫外到短波红外的光谱信息照片,提供更多的场景细节信息。

如表 1 所示,本文总结了代表性硫汞族胶体量子点单点探测器、焦平面阵列及红外-可见光上转换器件在探测波长、阵列规模、比探测率等核心参数指标性能对比。其中,F 和 S 分别代表焦平面阵列和单点探测器。

4 结束语

本文对硫汞族胶体量子点红外光电探测技术的研究现状进行了总结,综述了硫汞族胶体量子点探测器和硫汞族胶体量子点焦平面阵列的发展趋势及应用方向。在过去的十年间,硫汞族胶体量子点从单点探测器到焦平面阵列都有着巨大的突破。但是,硫汞族胶体量子点体系还面临着很多挑战,还有诸多亟待解决的问题以及值得探索的方向。在单点红外探测器方面,需要进一步优化材料的物性(例如提升载流子迁移率、优化表面缺陷等),提升探测器的光电响应性能,研究长波红外探测器,以及优化探测器结构等。对于上转换器件,需要进一步拓宽红外探测波段范围,提升红外光子-可见光子上转换效率,最终实现高分辨率、高灵敏度的红外上转换成像。对于焦平面阵列,目前的研究主要集中在开发具有高分辨率和低噪声的大阵列红外探测器,在航天、军工、工业检测、消费电子等领域均有着广泛的应用。宽光谱红外成像仪被用于半导体检测、医疗药物筛选和农产品观察。硫汞族胶体量子点作为一种液态半导体材料,无需倒装键合及像素对准,可与焦平面阵列读出电路表面像素电极实现直接电学耦合。与块状材料相比,硫汞族胶体量子点可以降低制造成本,扩大探测器的应用领域。总之,胶体量
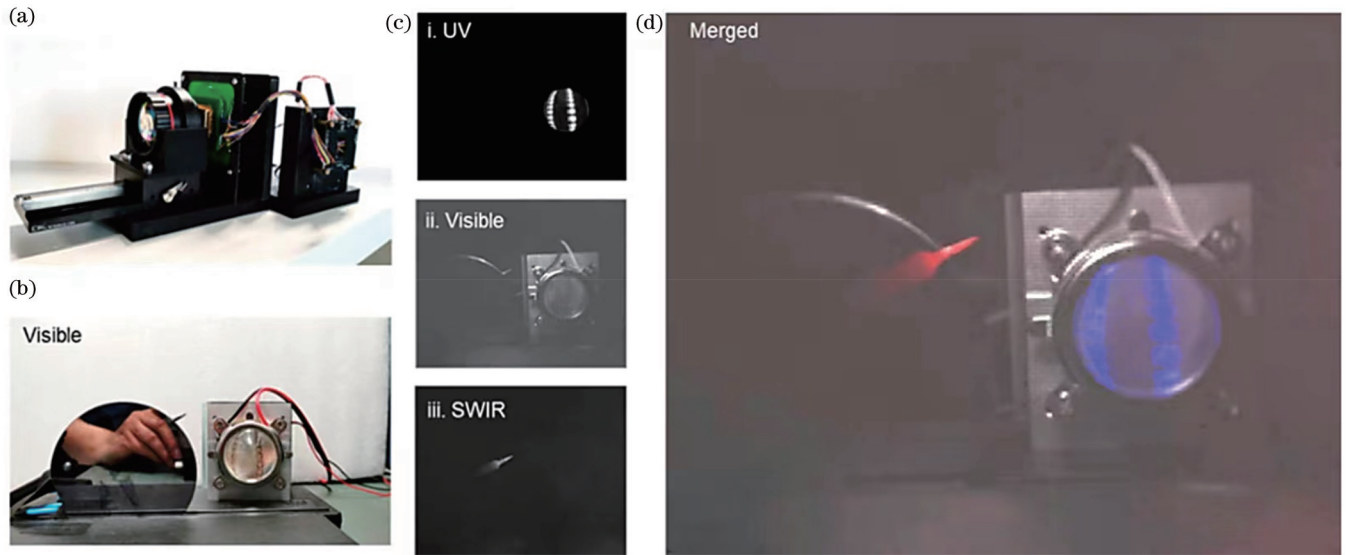
图 10　硫汞族胶体量子点红外焦平面阵列研究[54]。(a)多光谱胶体量子点成像仪及其外围电路;(b)成像场景:烙铁、硅片、紫外线灯;(c)获得的紫外、可见光和短波红外图像;(d)将紫外图像作为蓝色通道、可见光图像作为灰度通道、短波红外图像作为红色通道进行多光谱图像融合

Fig. 10　Study on infrared focal plane array based on mercury chalcogenide CQDs[54]. (a) Multispectral CQD imagers and periphery circuits; (b) imaging scene: a soldering iron, a silicon wafer, and an ultraviolet lamp; (c) captured ultraviolet, visible, and short-wave infrared images; (d) merged multispectral images with an ultraviolet image as the blue channel, visible light as the grayscale channel, and a short-wave infrared image as the red channel

表 1　不同类型量子点探测器的性能对比

Table 1　Device performance comparison of photodetectors with different configurations

Institute	Device configuration	Cut-off wavelength $\lambda_{\text{Cut-off}}$ /μm	Pixel array	Sensing material	Detectivity Jones	EQE /%	Responsivity A /W	Operating temperature /K
UChicago7	Interband	1.7-5	N/A	HgTe CQDs	S:109	N/A	S:0.25	130
UChicago16	Interband	5.25	N/A	HgTe CQDs	S:4.2×1010	2.5	S:0.08	90
Sorbonne52	Interband	2.0	640×512	HgTe CQDs	N/A	4-5	N/A	300
BIT53	Interband	2.5	320×256	HgTe CQDs	F:2×1011 S:6×1011	175	F:2.3 S:28	300
BIT54	Interband	2.5	320×256	HgTe CQDs	N/A	N/A	F:0.25	300
UChicago28	Intraband	5	N/A	HgSe CQDs	S:8.5×108	N/A	S:0.012	80
Sorbonne35	Intraband	5	N/A	HgTe and HgSe CQDs	S:109	N/A	S:0.003	80
BIT38	Intraband	5	N/A	HgSe CQDs	S:1.7×109	N/A	S:0.077	80
BIT35	Upconverter	2.5	N/A	HgTe CQDs	S:4.86×1010	92.71	1.85	300

Note: S represents single-point device, and F represents focal plane array.

子点技术是低成本、高性能红外探测器技术发展的必然趋势之一,相关研究成果将推动红外探测领域的发展,在应用方面不断激发新的可能。

参 考 文 献

[1] Rogalski A. Infrared detectors[M]. 2nd ed. Boca Raton: CRC Press, 2010.

[2] Rogalski A. HgCdTe infrared detector material: history, status and outlook[J]. Reports on Progress in Physics, 2005, 68(10): 2267-2336.

[3] Sargent E H. Infrared quantum dots[J]. Advanced Materials, 2005, 17(5): 515-522.

[4] Guyot-Sionnest P, Ackerman M M, Tang X. Colloidal quantum dots for infrared detection beyond silicon[J]. The Journal of Chemical Physics, 2019, 151(6): 060901.

[5] Tang X, Tang X B, Lai K W C. Scalable fabrication of infrared detectors with multispectral photoresponse based on patterned colloidal quantum dot films[J]. ACS Photonics, 2016, 3(12): 2396-2404.

[6] Zhang S, Hu Y, Hao Q. Advances of sensitive infrared detectors with HgTe colloidal quantum dots[J]. Coatings, 2020, 10(8): 760.

[7] Keuleyan S, Lhuillier E, Brajuskovic V, et al. Mid-infrared HgTe colloidal quantum dot photodetectors[J]. Nature Photonics, 2011, 5(8): 489-493.

[8] Chen M L, Lan X Z, Hudson M H, et al. Magnetoresistance of high mobility HgTe quantum dot films with controlled charging

[J]. Journal of Materials Chemistry C，2022，10(37): 13771-13777.

[9] Melnychuk C, Guyot-Sionnest P. Slow auger relaxation in HgTe colloidal quantum dots[J]. The Journal of Physical Chemistry Letters, 2018, 9(9): 2208-2211.

[10] Ackerman M M, Chen M L, Guyot-Sionnest P. HgTe colloidal quantum dot photodiodes for extended short-wave infrared detection[J]. Applied Physics Letters, 2020, 116(8): 083502.

[11] Tang X, Ackerman M M, Guyot-Sionnest P. Thermal imaging with plasmon resonance enhanced HgTe colloidal quantum dot photovoltaic devices[J]. ACS Nano, 2018, 12(7): 7362-7370.

[12] Shen G H, Guyot-Sionnest P. HgTe/CdTe and HgSe/CdX (X = S, Se, and Te) core/shell mid-infrared quantum dots[J]. Chemistry of Materials, 2019, 31(1): 286-293.

[13] Keuleyan S, Lhuillier E, Guyot-Sionnest P. Synthesis of colloidal HgTe quantum dots for narrow mid-IR emission and detection[J]. Journal of the American Chemical Society, 2011, 133(41): 16422-16424.

[14] Lhuillier E, Keuleyan S, Zolotavin P, et al. Mid-infrared HgTe/As$_2$S$_3$ field effect transistors and photodetectors[J]. Advanced Materials, 2013, 25(1): 137-141.

[15] Keuleyan S, Kohler J, Guyot-Sionnest P. Photoluminescence of mid-infrared HgTe colloidal quantum dots[J]. The Journal of Physical Chemistry C, 2014, 118(5): 2749-2753.

[16] Guyot-Sionnest P, Roberts J A. Background limited mid-infrared photodetection with photovoltaic HgTe colloidal quantum dots[J]. Applied Physics Letters, 2015, 107(25): 253104.

[17] Chen M L, Lan X Z, Tang X, et al. High carrier mobility in HgTe quantum dot solids improves mid-IR photodetectors[J]. ACS Photonics, 2019, 6(9): 2358-2365.

[18] Shen G H, Chen M L, Guyot-Sionnest P. Synthesis of nonaggregating HgTe colloidal quantum dots and the emergence of air-stable n-doping[J]. The Journal of Physical Chemistry Letters, 2017, 8(10): 2224-2228.

[19] Hudson M H, Chen M L, Kamysbayev V, et al. Conduction band fine structure in colloidal HgTe quantum dots[J]. ACS Nano, 2018, 12(9): 9397-9404.

[20] Lhuillier E, Keuleyan S, Guyot-Sionnest P. Optical properties of HgTe colloidal quantum dots[J]. Nanotechnology, 2012, 23(17): 175705.

[21] Ackerman M, Tang X, Guyot-Sionnest P. Fast and sensitive colloidal quantum dot mid-wave infrared photodetectors[J]. ACS Nano, 2018, 12(7): 7264-7271.

[22] Tang X, Ackerman M M, Chen M L, et al. Dual-band infrared imaging using stacked colloidal quantum dot photodiodes[J]. Nature Photonics, 2019, 13(4): 277-282.

[23] Zhang S, Chen M L, Mu G, et al. Spray-stencil lithography enabled large-scale fabrication of multispectral colloidal quantum-dot infrared detectors[J]. Advanced Materials Technologies, 2022, 7(6): 2101132.

[24] Zhao P F, Qin T L, Mu G, et al. Band-engineered dual-band visible and short-wave infrared photodetector with metal chalcogenide colloidal quantum dots[J]. Journal of Materials Chemistry C, 2023, 11(8): 2842-2850.

[25] Zhang S, Mu G, Cao J E, et al. Single-/ fused-band dual-mode mid-infrared imaging with colloidal quantum-dot triple-junctions[J]. Photonics Research, 2022, 10(8): 1987-1995.

[26] Luo Y N, Zhang S, Tang X, et al. Resonant cavity-enhanced colloidal quantum-dot dual-band infrared photodetectors[J]. Journal of Materials Chemistry C, 2022, 10(21): 8218-8225.

[27] Xue X M, Chen M L, Luo Y N, et al. High-operating-temperature mid-infrared photodetectors via quantum dot gradient homojunction[J]. Light: Science & Applications, 2023, 12: 2.

[28] Deng Z Y, Jeong K S, Guyot-Sionnest P. Colloidal quantum dots intraband photodetectors[J]. ACS Nano, 2014, 8(11):

11707-11714.

[29] Jeong K S, Deng Z Y, Keuleyan S, et al. Air-stable n-doped colloidal HgS quantum dots[J]. The Journal of Physical Chemistry Letters, 2014, 5(7): 1139-1143.

[30] Shen G H, Guyot-Sionnest P. HgS and HgS/CdS colloidal quantum dots with infrared intraband transitions and emergence of a surface plasmon[J]. The Journal of Physical Chemistry C, 2016, 120(21): 11744-11753.

[31] Robin A, Livache C, Ithurria S, et al. Surface control of doping in self-doped nanocrystals[J]. ACS Applied Materials & Interfaces, 2016, 8(40): 27122-27128.

[32] Martinez B, Livache C, Notemgnou Mouafo L D, et al. HgSe self-doped nanocrystals as a platform to investigate the effects of vanishing confinement[J]. ACS Applied Materials & Interfaces, 2017, 9(41): 36173-36180.

[33] Martinez B, Livache C, Meriggio E, et al. Polyoxometalate as control agent for the doping in HgSe self-doped nanocrystals[J]. The Journal of Physical Chemistry C, 2018, 122(46): 26680-26685.

[34] Livache C, Martinez B, Goubet N, et al. A colloidal quantum dot infrared photodetector and its use for intraband detection[J]. Nature Communications, 2019, 10: 2125.

[35] Khalili A, Weis M, Mizrahi S G, et al. Guided-mode resonator coupled with nanocrystal intraband absorption[J]. ACS Photonics, 2022, 9(3): 985-993.

[36] Chen M L, Shen G H, Guyot-Sionnest P. State-resolved mobility of 1 cm^2/(Vs) with HgSe quantum dot films[J]. The Journal of Physical Chemistry Letters, 2020, 11(6): 2303-2307.

[37] Chen M L, Shen G H, Guyot-Sionnest P. Size distribution effects on mobility and intraband gap of HgSe quantum dots[J]. The Journal of Physical Chemistry C, 2020, 124(29): 16216-16221.

[38] Chen M L, Hao Q, Luo Y N, et al. Mid-infrared intraband photodetector via high carrier mobility HgSe colloidal quantum dots[J]. ACS Nano, 2022, 16(7): 11027-11035.

[39] Tang X, Wu G F, Lai K W C. Plasmon resonance enhanced colloidal HgSe quantum dot filterless narrowband photodetectors for mid-wave infrared[J]. Journal of Materials Chemistry C, 2017, 5(2): 362-369.

[40] Tachibana H, Aizawa N, Hidaka Y, et al. Tunable full-color electroluminescence from all-organic optical upconversion devices by near-infrared sensing[J]. ACS Photonics, 2017, 4(2): 223-227.

[41] Li N, Lan Z J, Lau Y S, et al. SWIR photodetection and visualization realized by incorporating an organic SWIR sensitive bulk heterojunction[J]. Advanced Science, 2020, 7(14): 2000444.

[42] Ban D, Han S, Lu Z H, et al. Near-infrared to visible light optical upconversion by direct tandem integration of organic light-emitting diode and inorganic photodetector[J]. Applied Physics Letters, 2007, 90(9): 093108.

[43] Yeddu V, Seo G, Cruciani F, et al. Low-band-gap polymer-based infrared-to-visible upconversion organic light-emitting diodes with infrared sensitivity up to 1.1 µm[J]. ACS Photonics, 2019, 6(10): 2368-2374.

[44] Chen J, Tao J C, Ban D Y, et al. Hybrid organic/inorganic optical up-converter for pixel-less near-infrared imaging[J]. Advanced Materials, 2012, 24(23): 3138-3142.

[45] Liu H C, Li J, Wasilewski Z R, et al. Integrated quantum well intersub-band photodetector and light emitting diode[J]. Electronics Letters, 1995, 31(10): 832-833.

[46] Strassel K, Kaiser A, Jenatsch S, et al. Squaraine dye for a visibly transparent all-organic optical upconversion device with sensitivity at 1000 nm[J]. ACS Applied Materials & Interfaces, 2018, 10(13): 11063-11069.

[47] Yu B H, Cheng Y H, Li M L, et al. Sub-band gap turn-on near-infrared-to-visible up-conversion device enabled by an organic –

inorganic hybrid perovskite photovoltaic absorber[J]. ACS Applied Materials & Interfaces, 2018, 10(18): 15920-15925.

[48] Yang D Z, Zhou X K, Ma D G, et al. Near infrared to visible light organic up-conversion devices with photon-to-photon conversion efficiency approaching 30% [J]. Materials Horizons, 2018, 5(5): 874-882.

[49] Mu G, Rao T Y, Zhang S, et al. Ultrasensitive colloidal quantum-dot upconverters for extended short-wave infrared[J]. ACS Applied Materials & Interfaces, 2022, 14(40): 45553-45561.

[50] Ciani A J, Pimpinella R E, Grein C H, et al. Colloidal quantum dots for low-cost MWIR imaging[J]. Proceedings of SPIE, 2016, 9819: 981919.

[51] Buurma C, Pimpinella R E, Ciani A J, et al. MWIR imaging with low cost colloidal quantum dot films[J]. Proceedings of SPIE, 2016, 9933: 993303.

[52] Gréboval C, Darson D, Parahyba V, et al. Photoconductive focal plane array based on HgTe quantum dots for fast and cost-effective short-wave infrared imaging[J]. Nanoscale, 2022, 14(26): 9359-9368.

[53] Zhang S, Bi C, Qin T L, et al. Wafer-scale fabrication of CMOS-compatible trapping-mode infrared imagers with colloidal quantum dots[J]. ACS Photonics, 2023, 10(3): 673-682.

[54] Zhang S, Bi C, Tan Y M, et al. Direct optical lithography enabled multispectral colloidal quantum-dot imagers from ultraviolet to short-wave infrared[J]. ACS Nano, 2022, 16(11): 18822-18829.

Infrared Optoelectrical Detection Technology Based on Mercury Chalcogenide Colloidal Quantum Dots

Hao Qun[1,2,3*], Tang Xin[1,2,3], Chen Menglu[1,2,3]

[1]*School of Optics and Photonics, Beijing Institute of Technology, Beijing* 100081, *China*;

[2]*Beijing Key Laboratory for Precision Optoelectronic Measurement Instrument and Technology, Beijing* 100081, *China*;

[3]*Yangtze Delta Region Academy of Beijing Institute of Technology, Jiaxing* 314019, *Zhejiang, China*

Abstract

Significance   Infrared detectors play an important role in military and aerospace fields including guidance, remote sensing, and reconnaissance. At present, infrared detectors are mainly based on bulk semiconductor materials such as mercury cadmium telluride (HgCdTe), indium gallium arsenic (InGaAs), and indium antimonide (InSb). However, these materials need to be fabricated on a lattice-matched substrate by a high-cost epitaxially grown method and be integrated with readout circuits through complex flip-chip bonding technology, restricting the further improvement of imaging array scale and resolution. Thus, it is significant to develop new material systems to replace traditional bulk semiconductor materials, so as to achieve low-cost, large-scale, and high-resolution infrared detectors.

The colloidal quantum dots (CQDs), as new semiconductor nanocrystal materials, can achieve precise band-gap regulation in a wide spectrum due to the quantum confinement effect. Besides, CQDs can be synthesized on a large scale and at a low cost by liquid-phase chemical method. Furthermore, the liquid phase processing technology of CQDs enables direct on-chip electrical coupling with silicon readout circuits without the need for flip-bonding. Therefore, CQD materials have gained wide attention and made significant progress in infrared detection and imaging. Among them, mercury chalcogenide CQDs have been proven to have a wide range of infrared detection bands including short-wave, mid-wave, and long-wave infrared bands. Besides, two-color or multi-color band detection, focal plane array imaging, and infrared-to-visible upconverters based on mercury chalcogenide CQDs have been studied and exhibited excellent device performance. Although infrared optoelectrical detection technology based on mercury chalcogenide CQDs has been widely studied, there is a lack of review to summarize the recent works. Hence, it is important to summarize the existing research and propose the future development direction.

Progress   First, according to the absorption process of CQDs, the infrared detectors based on mercury chalcogenide CQDs can be divided into interband and intraband transition. The device performance including cut-off wavelength, detectivity, external quantum efficiency (EQE), and responsivity are summarized and compared, as shown in Figs. 2-6 and Table 1. In 2011, Guyot-Sionnest professor from the University of Chicago first reported the interband transition mid-wave infrared photodetector based on the mercury telluride (HgTe) CQDs, exhibiting the detectivity of 10^9 Jones. In 2014, the same team developed an intraband transition mid-wave infrared detector based on mercury selenide (HgSe) CQDs with a detectivity of 8.5×10^8 Jones at 80 K. On this basis, since 2020, the group from the Beijing Institute of Technology carried out systematic research on infrared detectors based on mercury chalcogenide CQDs and made breakthroughs in two-color or multi-color band detection. In 2022, the team developed a CQDs single-band short-wave

infrared imaging and fused-band imaging (short-wave and mid-wave infrared) dual-mode detector capable of detecting, separating, and fusing photons from various wavelength ranges using three vertically stacked CQD homojunction. The dual-mode detectors showed a detectivity of up to 8×10^{10} Jones at the fused-band mode and 3.1×10^{11} Jones at the single-band mode, respectively.

Infrared-to-visible upconverters converting low-energy infrared light to higher-energy visible light without bringing in complicated readout integrated circuits have triggered enormous excitement. In 2022, the group from the Beijing Institute of Technology reported the upconverters using HgTe CQDs as the sensing layer and extended the operation spectral ranges to short-wave infrared bands for the first time (Fig. 7). Besides, mercury chalcogenide CQDs play an important role in improving the resolution of infrared focal plane array (FPA) imagers because the pixel pitch is only determined by the readout circuit array. In 2016, the research team at the University of Chicago reported the first HgTe CQD mid-wave infrared FPA imagers with EQE of 0.30%, detectivity of 1.46×10^9 Jones, and noise equivalent temperature difference (NETD) of 2.319 K at the temperature of 95 K (Fig. 8). In 2022, the research team of Sorbonne University in France prepared photoconductive HgTe CQD FPA imagers of 1.8 μm through spin coating technology with 640×512 and pixel pitch of 15 μm (Fig. 8). On this basis, the group from the Beijing Institute of Technology continued to innovate in the field of mercury chalcogenide CQD FPA imagers. In 2022, a new device architecture of a trapping-mode detector was proposed and successfully utilized for HgTe CQD FPA imagers. The complementary metal oxide semiconductor (CMOS)-compatible HgTe CQD FPA imagers exhibit low photoresponse non-uniformity (PRNU) of 4%, dead pixel rate of 0%, high EQE of 175%, and high detectivity of 2×10^{11} Jones for extended short-wave infrared bands (cut-off wavelength is 2.5 μm) @ 300 K and 8×10^{10} Jones for mid-wave infrared bands (cut-off wavelength is 5.5 μm) @ 80 K (Fig. 9). Furthermore, high-resolution single-color images and merged multispectral images from ultraviolet to short-wave infrared bands were obtained by using direct optical lithography for FPA imagers based on HgTe CQDs (Fig. 10). The performance of mercury chalcogenide CQDs-based FPA imagers is summarized, as shown in Table 1. In the end, the problems faced and the ongoing research trends in this field are discussed.

Conclusions and Prospects　In the past decade, there have been great breakthroughs in mercury chalcogenide CQDs-based infrared detectors from single-pixel detectors to FPA imagers. In summary, the physical properties of mercury chalcogenide CQDs such as carrier mobility and device performance including response speed, infrared detection band range, detectivity, and photoresponse uniformity still need to be improved, so as to promote the development of mercury chalcogenide CQDs-based infrared detectors.

Key words　mercury chalcogenide colloidal quantum dots; infrared detectors; infrared focal plane array; infrared upconverter device